function in the nucleus as is demonstrated by the absence of spectinomycin resistance, despite the presence of a nuclear *aadA* gene in all of the kanamycin-resistant plants selected. □

Methods

pPRV111A::neoSTLS2 construction and transplastomic plants

pPRV111A::neoSTLS2 was produced by ligating the *Hin*dIII fragment containing *neoSTLS2* from plasmid pCMneoSTLS2 (ref. 13) into pPRV11A[14]. This transformation vector was introduced into the plastids of *Nicotiana tabacum* L. Petit Havana (N,N) by biolistic bombardment, and homoplasmic plants were regenerated as described previously[14]. The homoplasmic plants were transferred to soil and grown in a controlled environment chamber with a 14 h light/10 h dark and 25 °C day/20 °C night growth regime. The photon flux density was approximately 300 μmol m^{-2} s^{-1} at the plant surface. The nuclear *neoSTLS2* control line was generated by biolistic bombardment with plasmid pCMneoSTLS2 (ref. 13).

Seedling tests for resistance to kanamycin and spectinomycin

Surface-sterilized seeds were plated on 150-mm plates containing 50 ml of 0.5 MS salt medium[25] and either spectinomycin dihydrochloride (500 μg ml^{-1}) or kanamycin sulphate (150 μg ml^{-1}). For screening seeds of self-pollinated tp7, the latter medium was supplemented with geneticin disulphate (20 μg ml^{-1}) when seedlings were two weeks old. The plates were placed at 25 °C with continuous fluorescent light. To determine nondestructively the kanamycin-resistance phenotype for verification of transplastomic/ nuclear junctions, leaf pieces were taken from individual seedlings grown in 0.5 MS medium without kanamycin, and then cultured in MS medium containing 150 μg ml^{-1} kanamycin and the required plant hormones[25]. Kanamycin resistance was judged by callus growth.

Molecular analysis

DNA and RNA blot analyses were carried out as described[11,26]. Junction sequences were obtained using iPCR as described (see http://arabi4.agr.hokudai.ac.jp/ArabiE/protocols/ general/general.html). Key differences in the restriction fragment sizes between nuclear and transplastomic DNA were used to design cpDNA primers adjacent to the site of integration. These primers were used in conjunction with a second primer specific for either *aadA* or *neoSTLS2*. Primers used in iPCR were 5′-GAAGTTTCCAAAAGGTCGTT-3′ with 5′-CTCGCCATCTATTTTCATTG-3′ for kr1, 5′-CCAGATTCCAAATGAACAAA-3′ (f2) with 5′-CAATAGCCCTCTGGTCTTCT-3′ (r3) for kr17, and f2 with r3 for kr18. PCR amplification[11] of the junction sequences was undertaken with primers 5′-GCACTGTGTCATTCAATACT-3′ (f1) and 5′-CCAATTGTGACATCCCTTCT-3′ (r1) for kr1, f2 and 5′-GGTTTTCCAAAGGGGTTTT-3′ (r2) for kr17, and 5′-GCCGTCATCAC TAACCATT-3′ (f3) and r3 for kr18.

1. Martin, W. et al. Evolutionary analysis of *Arabidopsis*, cyanobacterial, and chloroplast genomes reveals plastid phylogeny and thousands of cyanobacterial genes in the nucleus. *Proc. Natl Acad. Sci. USA* **99**, 12246–12251 (2002).
2. Kaneko, T. et al. Sequence analysis of the genome of the unicellular cyanobacterium *Synechocystis* sp. strain PCC6803. II. Sequence determination of the entire genome and assignment of potential protein-coding regions. *DNA Res.* **3**, 109–136 (1996).
3. Gray, M. W. The endosymbiont hypothesis revisited. *Int. Rev. Cytol.* **141**, 233–357 (1992).
4. Adams, K. L., Daley, D. O., Qiu, Y. L., Whelan, J. & Palmer, J. D. Repeated, recent and diverse transfers of a mitochondrial gene to the nucleus in flowering plants. *Nature* **408**, 354–357 (2000).
5. Millen, R. S. et al. Many parallel losses of *inf*A from chloroplast DNA during angiosperm evolution with multiple independent transfers to the nucleus. *Plant Cell* **13**, 645–658 (2001).
6. Stupar, R. M. et al. Complex mtDNA constitutes an approximate 620-kb insertion on *Arabidopsis thaliana* chromosome 2: implication of potential sequencing errors caused by large-unit repeats. *Proc. Natl Acad. Sci. USA* **98**, 5099–5103 (2001).
7. Yuan, Q. et al. Genome sequencing of 239-kb region of rice chromosome 10L reveals a high frequency of gene duplication and a large chloroplast DNA insertion. *Mol. Genet. Gen.* **267**, 713–720 (2002).
8. Timmis, J. N. & Scott, N. S. Spinach nuclear and chloroplast DNAs have homologous sequences. *Nature* **205**, 65–67 (1983).
9. Mourier, T., Hansen, A. J., Willerslev, E. & Arctander, P. The human genome project reveals a continuous transfer of large mitochondrial fragments to the nucleus. *Mol. Biol. Evol.* **18**, 1833–1837 (2001).
10. Ricchetti, M., Fairhead, C. & Dujon, B. Mitochondrial DNA repairs double-strand breaks in yeast chromosomes. *Nature* **402**, 96–100 (1998).
11. Ayliffe, M. A. & Timmis, J. N. Tobacco nuclear DNA contains long tracts of homology to chloroplast DNA. *Theor. Appl. Genet.* **85**, 229–238 (1992).
12. Thorsness, P. E. & Fox, T. D. Escape of DNA from the mitochondria to the nucleus in the yeast, *Saccharomyces cerevisiae. Nature* **346**, 376–379 (1990).
13. Maas, C. et al. Expression of intron modified *NPT*II genes in monocotyledonous and dicotyledonous plant cells. *Mol. Breed.* **3**, 15–28 (1997).
14. Zoubenko, O. V., Allison, L. A., Svab, Z. & Maliga, P. Efficient targeting of foreign genes into the tobacco plastid genome. *Nucleic Acids Res.* **22**, 3819–3824 (1994).
15. Benfey, P. N. & Chua, N. H. The cauliflower mosaic virus 35S promoter: combinatorial regulation of transcription in plants. *Science* **250**, 959–966 (1990).
16. Eckes, P., Rosahl, S., Schell, J. & Willmitzer, L. Isolation and characterization of a light-inducible, organ-specific gene from potato and analysis of its expression after tagging and transfer into tobacco and potato shoots. *Mol. Gen. Genet.* **205**, 14–22 (1986).
17. Whitney, S. M. & Andrews, T. J. The gene for the ribulose-1, 5-bisphosphate carboxylase/oxygenase (Rubisco) small subunit relocated to the plastid genome of tobacco directs the synthesis of small subunits that assemble into Rubisco. *Plant Cell* **13**, 193–205 (2001).
18. Horser, C., Abbott, D., Wesley, V., Smith, N. & Waterhouse, P. Gene silencing—principles and application. *Genet. Eng. Principles Meth.* **24**, 239–256 (2002).
19. Daniell, H., Datta, R., Varma, S., Gray, S. & Lee, S. B. Containment of herbicide resistance through genetic engineering of the chloroplast genome. *Nature Biotechnol.* **16**, 345–348 (1998).
20. Fagard, M. & Vaucheret, H. (Trans)gene silencing in plants: how many mechanisms? *Annu. Rev. Plant Physiol. Plant Mol. Biol.* **51**, 167–194 (2000).
21. Babiychuk, E., Fuangthong, M., van Montagu, M., Inzé, D. & Kushnir, S. Efficient gene tagging in *Arabidopsis thaliana* using a gene trap approach. *Proc. Natl Acad. Sci. USA* **94**, 12722–12727 (1997).
22. Maliga, P. Engineering the plastid genome of higher plants. *Curr. Opin. Plant Biol.* **5**, 164–172 (2002).
23. Daniell, H., Khan, M. S. & Allison, L. Milestones in chloroplast genetic engineering: an environmentally friendly era in biotechnology. *Trends Plant Sci.* **7**, 84–91 (2002).
24. Scott, S. E. & Wilkinson, M. J. Low probability of chloroplast movement from oilseed rape (*Brassica napus*) into wild *Brassica rapa. Nature Biotechnol.* **17**, 390–392 (1999).
25. Murashige, T. & Skoog, F. A revised medium for rapid growth and bioassays with tobacco tissue cultures. *Physiol. Plant* **15**, 473–497 (1962).
26. Huang, C. Y., Barker, S. J., Langridge, P., Smith, F. W. & Graham, R. D. Zinc deficiency up-regulates expression of high-affinity phosphate transporter genes in both phosphate-sufficient and -deficient barley roots. *Plant Physiol.* **124**, 415–422 (2000).

....

Optimal transsaccadic integration explains distorted spatial perception

Matthias Niemeier*†‡, **J. Douglas Crawford**†‡ & **Douglas B. Tweed***†‡

* *Departments of Physiology and Medicine, University of Toronto, 1 King's College Circle, Toronto M5S 1A8, Canada*
† *Canadian Institutes of Health Research, Group for Action and Perception*
‡ *Centre for Vision Research, York University, 4700 Keele Street, Toronto M3J 1P3, Canada*

....

We scan our surroundings with quick eye movements called saccades, and from the resulting sequence of images we build a unified percept by a process known as transsaccadic integration. This integration is often said to be flawed, because around the time of saccades, our perception is distorted[1–6] and we show saccadic suppression of displacement (SSD): we fail to notice if objects change location during the eye movement[7,8]. Here we show that transsaccadic integration works by optimal inference. We simulated a visuomotor system with realistic saccades, retinal acuity, motion detectors and eye-position sense, and programmed it to make optimal use of these imperfect data when interpreting scenes. This optimized model showed human-like SSD and distortions of spatial perception. It made new predictions, including tight correlations between perception and motor action (for example, more SSD in people with less-precise eye control) and a graded contraction of perceived jumps; we verified these predictions experimentally. Our results suggest that the brain constructs its evolving picture of the world by optimally integrating each new piece of sensory or motor information.

We make two or three saccades per second, collecting a rapid series of visual snapshots of the world. To perceive a large, changing scene—for example, when navigating through traffic—we mentally join up the images like pieces of a spatiotemporal jigsaw puzzle. To work out which piece of the puzzle goes where, the brain uses information from three main sources, all of them imperfect. One source is the retinal locations of images, but retinal acuity declines with eccentricity[9,10]. The second source is the velocity signals from visual motion detectors; these are accurate when the eyes are stationary[11,12], but ineffective during saccades[13–16]. The third is our sense of eye position, derived from muscle spindles[17] or motor commands[18–20], but this information is also imperfectly reliable, especially during saccades[21,22].

Is it possible that transsaccadic integration uses its limited inputs in an optimal way, despite apparent flaws such as SSD? To see what optimal integration would look like, we simulated a visuomotor system that receives these three signals. It makes saccades, and

sometimes during or between those saccades, an object in its visual field jumps to a new location. The system judges whether a jump has occurred, and estimates its size and direction. For its deductions, the system knows the probability distributions of its unreliable signals, and of its own saccades and of jumps in the world. It makes optimal use of all its information to deduce the events in its surroundings (see Methods).

We simulated the model's performance in a typical psychophysical experiment: guessing in which of two possible directions a spot has jumped. Figure 1a plots the model's probability of choosing correctly as a function of jump size. If the spot jumps when the eye is stationary, the model (dotted line) notices: its perceptual threshold, defined as the smallest jump whose direction it can guess correctly 75% of the time, is very low. If the spot jumps during a saccade, the threshold is higher[7] and it increases with saccade amplitude[8]. As shown in the inset, this increase is approximately linear, also in agreement with published data[23,24]. Our own subject in Fig. 1b, given the same tasks, shows the same behaviours. Thus, optimal transsaccadic integration results in SSD, and in a human-like way. So, SSD need not reflect flawed transsaccadic integration, but is an unavoidable consequence of optimal inference from imperfect signals.

To test this model further, we used it to generate new predictions about SSD. The model shows SSD for two reasons, the first being that it attributes apparent jumps to errors in its visual and motor signals; therefore, it will show more SSD the more uncertain it is about its sensorimotor data. If its eye-position sense, like that of humans[21], is less reliable parallel to a saccade than orthogonal to it, then it will be more blind to target jumps in the parallel dimension. This behaviour is shown in Fig. 1c, in which the model senses smaller jumps orthogonal to its saccades (dashed line) than parallel to them (solid line). To test this prediction experimentally, we had seven people perform the same tasks (see Methods). Like the typical subject in Fig. 1d, all subjects matched the model's predictions: they showed much less SSD for orthogonal than for parallel jumps ($P = 0.004$).

Also according to the model, SSD in any direction should depend on the combined uncertainty of retinal localization and eye-position sense in that direction. We can estimate this uncertainty by measuring the scatter (the standard deviation, s.d.) of eye positions right after the saccade (see Methods); we would expect a person's SSD to correlate with the postsaccadic scatter of their eye positions. The model predicts tighter correlations if we 'cancel out' other intersubject differences by taking ratios, as shown in Fig. 2a. Here, the variable on the abscissa is the 'eye-position scatter ratio'; for example, if after saccades your eye positions are spread out three times as much in the direction of the saccade than in the orthogonal
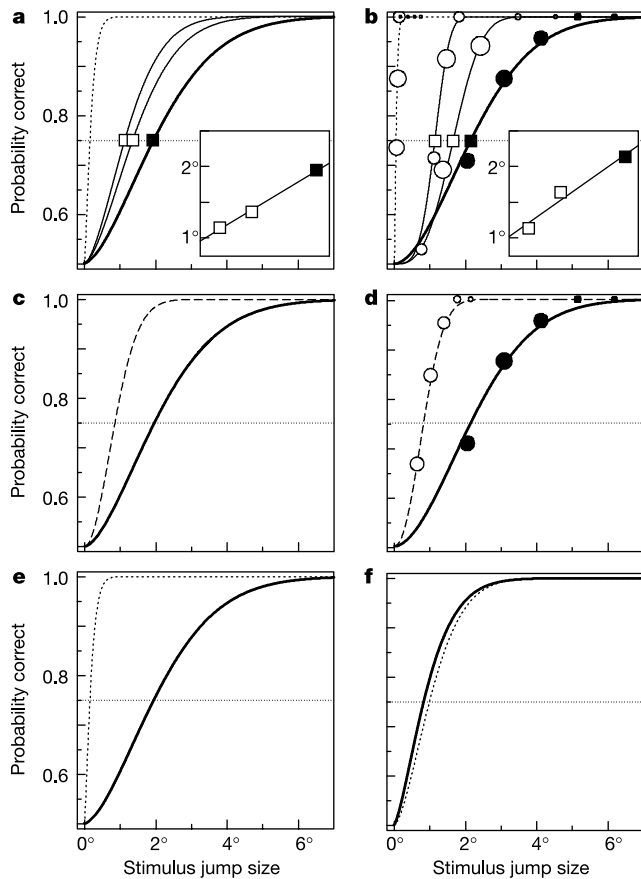

Figure 1 Predicted and actual saccadic suppression of displacement (SSD). **a**, The model judges in which of two directions a spot has jumped. If the spot jumps when the eye is fixating (dotted line), the threshold of perception (the jump size at which the model guesses the direction correctly 75% of the time) is just 0.2°. During 7.5° saccades (thin solid line), the threshold increases to 1.1°; during 10° saccades (medium solid line), it rises to 1.4°; and with 15° saccades (thick solid line), to 2°. The inset plots thresholds as a function of saccade size. **b**, A human subject's judgements on the same tasks. **c**, In the model, thresholds are lower for jumps orthogonal to the saccade (dashed line) than for parallel jumps (solid line). **d**, On the same tasks, a typical subject shows the same behaviour. Areas of circles represent the numbers of trials for each jump size. **e**, Simulating the blanking effect. When the target is continuously presented, the model shows low thresholds during fixation (dotted line) and high thresholds during saccades (solid line). **f**, When the target is blanked, the thresholds shift in opposite directions.
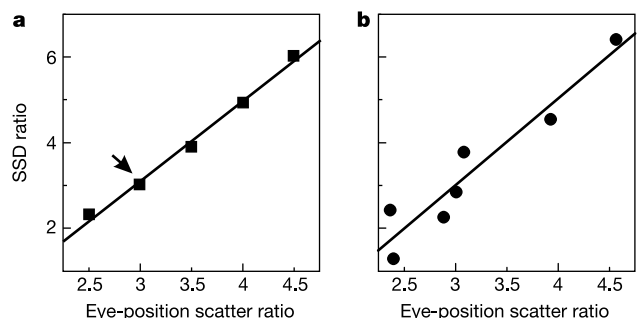

Figure 2 Perception and motor control. **a**, The optimal-integration model predicts a monotonic, roughly linear relationship between sensorimotor uncertainty, as reflected in eye-position scatter ratios, and SSD ratios (see text). **b**, Data from seven subjects confirm the prediction. Lines in both plots are best-fit linear regressions.
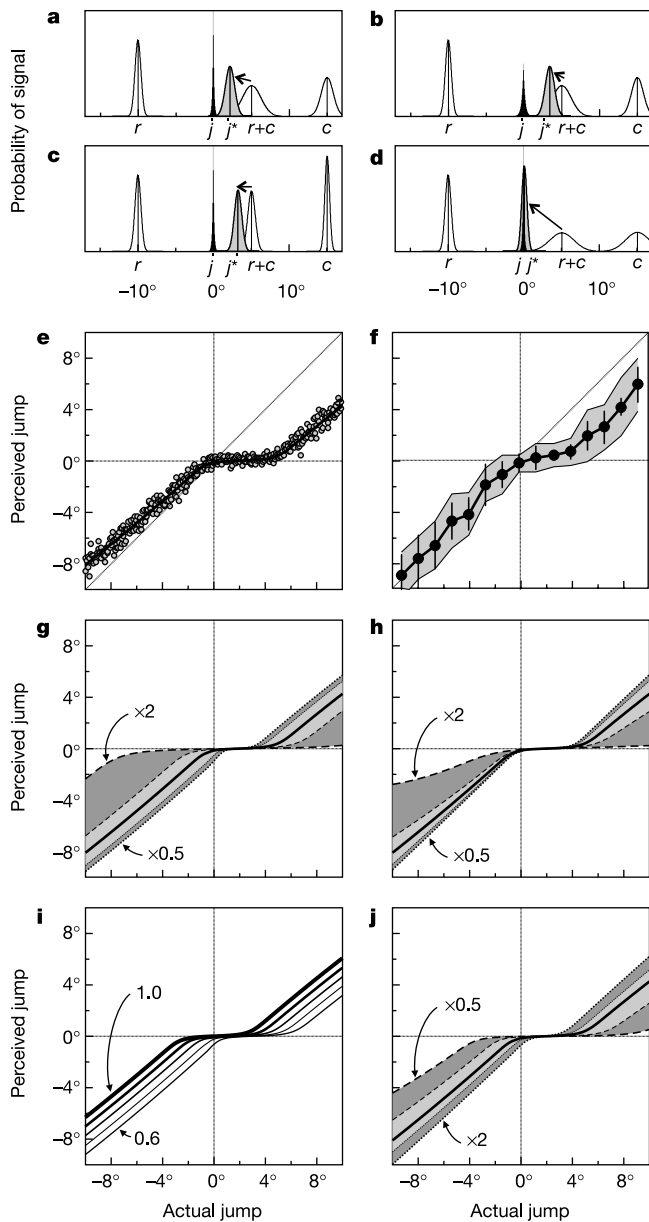
Figure 3 Contraction of perceived jumps. **a**, The percept j^* reflects a tug of war between the prior probability of a jump, j, and the sensorimotor estimate $r + c$, where r is the retinal signal and c is the efference copy signal; during saccades, v (an independent estimate derived from visual velocity detectors of the change in retinal location) has no role. **b**, **c**, j^* stays closer to $r + c$ when the prior probability of non-zero jumps is higher (that is, when $p(j)$ is wider; **b**), or when r and c are less variable (and therefore more reliable; **c**). **d**, But when r and c are highly variable, j^* gravitates strongly towards zero. **e**, The model predicts contraction: the slope of the curve is shallow near the middle. Grey circles are 1,000 responses, after 15° saccades. The solid line indicates average model performance; the straight diagonal line, ideal perception. **f**, All eight subjects showed similar contraction; this graph shows their bin-wise averaged responses, with standard deviation (s.d.) bars and averages of the individual s.d.s (grey envelope). Remaining panels illustrate the sensitivity of j^* to the model's main parameters. **g**, Influence of eye-position uncertainty, σ_c. The thick solid curve is the model's performance when $\sigma_c = 2.5(0.01d + 0.05°)$, where d is the target distance (see Methods). Other curves show the results when this σ_c is multiplied by 2 and 1.3 (dashed lines), and by 0.7 and 0.5 (dotted line). **h**, Retinal-shift uncertainty, σ_r. Thick curve: $\sigma_r = 0.02e + 0.15°$, where e is the postsaccadic, or postjump, eccentricity of the target. Other curves: σ_r multiplied by 2, 1.3, 0.7 and 0.5. **i**, Underestimation of saccade size, D. With more pronounced underestimation, the j^* curve shifts in the direction of the saccade. From left to right, $D = 1, 0.9, 0.8, 0.7$ and 0.6. **j**, Width of the probability density function $p(j)$. The thick curve is the model's performance when the width parameter, w, is 0.065°. For the other curves, w was multiplied by 0.5, 0.7, 1.3 and 2.

direction, then your scatter ratio is 3, as it is for the simulated person marked with an arrow in the figure. On the ordinate is the 'SSD ratio': if your threshold for sensing a target jump is three times as large when the jump is parallel to your saccade than when it is orthogonal, then your SSD ratio is 3, as it is for the same data point in Fig. 2a. The key prediction, shown in the graph, is that people with higher scatter ratios should have higher SSD ratios: the latter ratio should rise as a function of the former, monotonically and roughly linearly.

We tested this prediction on seven people. The results, given in Fig. 2b, confirm the model's predictions: subjects with larger scatter ratios had larger SSD ratios, with a correlation of $r = 0.95$ ($P < 0.01$). The human data in Fig. 2b followed a rising, roughly linear curve like those of the optimal integrators in Fig. 2a.

To generate further tests, we turned to the second reason the model shows SSD: namely, the sheer implausibility, outside a vision laboratory, of an otherwise stationary object jumping in perfect synch with a saccade. Because of this prior improbability, the optimal integrator distrusts its inputs when they signal a jump. So, the model implies that SSD should diminish when the context makes jumps more plausible. For example, it concurs with the finding of Gysen et al.[25] that SSD is reduced if the object is already moving before it jumps. And it fits Deubel and colleagues' observation[26] that SSD is reduced when the jumping object is blanked for a time before it reappears in its new location (blanking makes it plausible that the postsaccadic spot is a new object in a new location, or that the object passed behind a barrier and re-emerged later, both of which scenarios are more likely than an abrupt translocation). To simulate this, we programmed our model to regard apparent jumps as more plausible when they coincided with brief disappearances. The simulations (Fig. 1e–f) mimic the reduced SSD reported by Deubel et al.[26], and their observation that blanking makes jumps less perceptible when the eye is stationary (because motion cues are removed).

Previous accounts of SSD have considered only two-alternative tasks in which subjects detect jumps or judge their directions, but the optimal-integration model also predicts a graded contraction of perceived jumps. The mechanism is illustrated in Fig. 3a–d. In Fig. 3a, the efference copy signal, c, reports a saccade of 15° while the retina, r, reports a stimulus shift of $-10°$, although both reports carry some uncertainty, as represented by the gaussian distributions. Together, these two signals imply that the object has jumped $r + c = 15° - 10° = 5°$. But the prior probability of a jump, j, (black distribution marked j) is small away from zero, so the percept, j^*, is 'pulled' towards zero. The degree of pull depends on the widths of the c, r and j distributions (Fig. 3b–d).

Simulations indicate that perceived jumps should be a nonlinear function of actual jump size (Fig. 3e). Around zero, the graph runs almost horizontally, indicating strong contraction. Also, the graph is shifted in the direction of the saccade, because immediately after a saccade, the eye-position signal c is hypometric[22]. We tested these predictions experimentally. Eight subjects made saccades towards a target that jumped parallel to the saccade. Using a mouse, they then moved the target back to what they felt was its presaccadic position, thereby indicating the perceived jump size. As in the simulations, all subjects showed a contracted and shifted percept (Fig. 3f).

Studies have revealed various patterns of compression and shift in perisaccadic spatial percepts, similar but not identical to those in Fig. 3f, for paradigms more complex than our continuous presentation of a single visible target[1–6]. These tasks are beyond the current scope of our model, because some involve multiple visible objects, which complicate the probabilities, and all use a flashed target, whose perisaccadic localization requires precise judgements of timing and which the brain may interpret as a new, second object rather than as a reappearance of the presaccadic target, again affecting its probable location. For simplicity, the model considers just one object and two time points (pre- and postsaccade), but the

principle of optimal integration could be extended to deal with more complex conditions.

Our model of transsaccadic integration reconciles and clarifies previous approaches. It shows that the brain uses eye-position signals in interpreting retinal information[18], but only to a limited extent[27]. Our simulations show that SSD arises from noisy sensorimotor signals[7,23] and from the prior implausibility of sudden jumps during saccades[28]. And we show that optimal integration can explain both SSD and graded distortions of spatial perception.

These findings support a view in which the brain pieces together a coherent percept of the world like a probabilistic, spatiotemporal jigsaw puzzle. The computations are complex, but they could be learned from available sensory and motor signals (they are well approximated by artificial networks of just a few hundred sigmoid neurons). We suggest that natural selection and learning shape the brain's circuits into transsaccadic integrators that make optimal use of each piece of sensorimotor information. □

Methods

Optimal transsaccadic integration

For a full account of the optimized visuomotor model and its derivation, see Supplementary Information. The system receives three input variables: r is the change in the target's retinal location, before and after the saccade; v is an independent estimate of that change in retinal location derived from visual velocity detectors; c is the estimated change in eye position, conveyed by efference copy or proprioception. These signals are influenced by two other variables, s and j, which represent saccades and jumps; that is, the amplitudes and directions of sudden movements of the visible object. From c, r and v, the system guesses j. Using Bayes' rule and other laws of probability, it can be shown that the optimal estimate, $j^{\star}$ (the one that will yield the smallest misjudgement of j on average), is the ratio of two iterated integrals:

$$j^{\star} = \int \mathrm{d}j\, j \int \mathrm{d}s\, p(s)p(j)p(c|s)p(r|js)p(v|js)\Big/$$
$$\int \mathrm{d}j \int \mathrm{d}s\, p(s)p(j)p(c|s)p(r|js)p(v|js)$$
(1)

Here, each p is a probability density function; for example, $p(r|js)$ is the conditional probability density that the retinal shift would have value r if the jump had value j and the saccade had value s.

All distributions in the model are realistic, insofar as the real parameters are known, although at present, $p(j)$ and $p(r|js)$ can only be estimated. $p(s)$ is gaussian, with s.d. $\sigma_s = 0.01d + 0.05°$ (where d is the target distance) orthogonal to the saccade[29]; to simulate parallel scatter, we multiplied this value by the scatter ratios 2.5, 3, 3.5, 4 and 4.5 (compare Fig. 2a). Mean saccade size μ_s is equal to the target distance minus an undershoot, u, which is well approximated in our data by $u = 0.23\sigma_s + 0.41°$. $p(j)$ is a Laplace distribution, $\exp(-|j|/w)/2w$, where w is a free parameter that we set to 0.065° normally, and to 0.13° in the presence of blanking in Fig. 1f. $p(c|s)$, $p(r|js)$ and $p(v|js)$ are all gaussian. Because c is delayed and therefore hypometric right after saccades[22], $\mu_c = Ds$ (where D, the factor by which saccade size is underestimated, varies between about 0.75 and 0.9); we set $\sigma_c = \sigma_s$. For r, we set $\mu_r = j - s$ and $\sigma_r = 0.02e + 0.15°$, where e is the postsaccadic, or postjump, eccentricity of the target (initial eccentricity was constant for any one experiment). And for v, we set $\mu_v = r$ when there was no saccade, and $\mu_v = 0$ otherwise; we set σ_v at 0.005° (ref. 12). To simulate neural variability in the integrator itself, we added gaussian noise of s.d. 0.004 radians to $j^{\star}$. Moderate changes in these parameters do not affect the qualitative predictions—such as SSD, shifts and compression—and the linear relationships in Figs 1a and 2.

Experiments

Seven subjects with normal or corrected-to-normal vision participated in the first experiment. They sat in a dark room with their head stabilized on a bite-bar, and viewed computer-generated stimuli ($20\,\mathrm{cd\,m^{-2}}$) back-projected onto a 1.4-by-1.9-m screen spanning about 100° horizontally and 90° vertically. At the start of each trial, the subject fixated a small dot, 0.4° across, at one of four possible locations, at the corners of an imaginary central 10°-by-10° square (rather than straight ahead, so subjects could not tell the direction of the target's subsequent jump by its final location relative to the midline of the head). After 0.5–1 s, the fixation dot vanished and a target spot, 0.8° across, appeared 15° to the left, right, above or below fixation. Subjects looked to the target as quickly as possible. The computer, monitoring eye position from search-coil signals at 1,000 Hz, detected the saccade (eye velocity, $\geq 36° \mathrm{s}^{-1}$; eye position, $\geq 1.5°$ from the fixation point) and moved the target horizontally or vertically; 200 ms later, the screen went white and the subjects chose the direction in which they believed the target had jumped. An adaptive algorithm[30] varied the jump from trial to trial, mapping out the thresholds of perception. Thresholds differed for onward versus backward jumps, as predicted by the model; Fig. 2 is based on thresholds for pooled onward and backward jumps, but data and model agreed equally well when we separated these jump directions.

We switched off the fixation dot so that subjects could not use its direction relative to the target to perceive orthogonal jumps. Others have found reduced SSD orthogonal to

saccades, although their effects were smaller than ours, probably for other, methodological reasons[7].

In Fig. 2b, we quantified our subjects' uncertainty about eye and target position using scatter ratios. We validated this method with a study identical to the first, except that the target vanished at the start of the saccade. Subjects made as many corrective saccades as they wished, then pressed a button when they felt they were looking at the former location of the target. Clearly, the scatter of eye positions at this moment reflected the subject's uncertainty about the placement of eye and target. But the scatter ratios at that moment correlated tightly ($r = 0.93$, $P < 0.05$) with scatter ratios after the initial saccade, before any corrective movements. This shows that we can take, as an accurate measure of uncertainty, the scatter ratio after initial, uncorrected saccades, as we did in Fig. 2b.

The experiments on graded contraction of jumps were again identical to the first study, except that eight subjects made horizontal saccades to a target that jumped, during the saccade, to a location chosen randomly from a horizontal range of ±10°; 200 ms after the saccade, the target was replaced by a vertical bar that the subject moved to what they felt was the target's presaccadic location. Only one object was visible at any one time. In other experiments, subjects moved the target itself rather than a bar, but the results were the same.

1. Matin, L. & Pearce, D. G. Visual perception of direction for stimuli flashed during voluntary saccadic eye movements. *Science* **148**, 1485–1488 (1965).
2. Honda, H. Saccade-contingent displacement of the apparent position of visual stimuli flashed on a dimly illuminated structured background. *Vision Res.* **33**, 709–716 (1993).
3. Ross, J., Morrone, M. C. & Burr, D. C. Compression of space before saccades. *Nature* **386**, 598–601 (1997).
4. Morrone, M. C., Ross, R. & Burr, D. C. Apparent position of visual targets during real and simulated saccadic eye movements. *J. Neurosci.* **17**, 7941–7953 (1997).
5. Cai, R. H., Pouget, A., Schlag-Rey, M. & Schlag, J. Perceived geometrical relationships affected by eye-movement signals. *Nature* **386**, 601–604 (1997).
6. Lappe, M., Awater, H. & Krekelberg, B. Postsaccadic visual references generate presaccadic compression of space. *Nature* **403**, 892–895 (2000).
7. Mack, A. An investigation of the relationship between eye and retinal image movement in the perception of movement. *Percept. Psychophys.* **8**, 291–298 (1970).
8. Bridgeman, B., Hendry, D. & Stark, L. Failure to detect displacement of the visual world during saccadic eye movements. *Vision Res.* **15**, 719–722 (1975).
9. Westheimer, G. Spatial vision. *Annu. Rev. Psychol.* **35**, 201–226 (1984).
10. Carpenter, R. H. S. in *Vision and Visual Dysfunctions* (ed. Carpenter, R. H. S.) 1–10 (Macmillan, Boca Raton, 1991).
11. Choudhury, B. P. & Crossey, A. D. Slow-movement sensitivity in the human field of vision. *Physiol. Behav.* **26**, 125–128 (1981).
12. Tynan, P. D. & Sekuler, R. Motion processing in peripheral vision: Reaction time and perceived velocity. *Vision Res.* **22**, 61–68 (1982).
13. Burr, D. C., Holt, J., Johnstone, J. R. & Ross, J. Selective depression of motion sensitivity during saccades. *J. Physiol. (Lond.)* **333**, 1–15 (1982).
14. Burr, D. C., Morrone, M. C. & Ross, J. Selective suppression of the magnocellular visual pathway during saccadic eye movements. *Nature* **371**, 511–513 (1994).
15. Shiori, S. & Cavanagh, P. Saccadic suppression of low-level motion. *Vision Res.* **29**, 915–928 (1989).
16. Ilg, U. & Hoffmann, K.-P. Motion perception during saccades. *Vision Res.* **33**, 211–220 (1993).
17. Steinbach, M. J. Proprioceptive knowledge of eye position. *Vision Res.* **27**, 1737–1744 (1986).
18. von Helmholtz, H. *Handbuch der physiologischen Optik* (Leopold Voss, Hamburg and Leipzig, 1910).
19. von Holst, E. & Mittelstaedt, H. Das Reafferenzprinzip (Wechselwirkung zwischen Zentralnervensystem und Peripherie). *Naturwissenschaften* **37**, 464–476 (1950).
20. Sperry, R. W. Neural basis of the spontaneous optokinetic response produced by visual inversion. *J. Comp. Physiol. Psychol.* **43**, 482–489 (1950).
21. Dassonville, P., Schlag, J. & Schlag-Rey, M. Oculomotor localization relies on a dampened representation of saccadic eye movement displacement in human and nonhuman primates. *Vis. Neurosci.* **9**, 261–269 (1992).
22. Honda, H. Interaction of extraretinal eye position signals in a double-step saccade task: Psychophysical estimation. *Exp. Brain Res.* **113**, 327–336 (1997).
23. Li, W. & Matin, L. The influence of saccade length on the saccadic suppression of displacement detection. *Percept. Psychophys.* **48**, 453–458 (1990).
24. Li, W. & Matin, L. Saccadic suppression of displacement: Separate influences of saccade size and of target retinal eccentricity. *Vision Res.* **37**, 1779–1797 (1997).
25. Gysen, V., De Graef, P. & Verfaillie, K. Detection of intrasaccadic displacements and depth rotations of moving objects. *Vision Res.* **42**, 379–391 (2002).
26. Deubel, H., Schneider, W. X. & Bridgeman, B. Postsaccadic target blanking prevents saccadic suppression of image displacement. *Vision Res.* **36**, 985–996 (1996).
27. Bridgeman, B., Van der Heijden, A. H. C. & Velichkovsky, B. M. A theory of visual stability across saccadic eye movements. *Behav. Brain Sci.* **17**, 247–292 (1994).
28. MacKay, D. M. in *Handbook of Sensory Physiology* Vol. VII/3 (ed. Jung, R.) 307–332 (Springer, Berlin, 1973).
29. Van Opstal, A. J. & Van Gisbergen, J. A. M. Scatter in the metrics of saccades and properties of the collicular motor map. *Vision Res.* **29**, 1183–1196 (1989).
30. Kontsevich, L. L. & Tyler, C. W. Bayesian adaptive estimation of psychometric slope and threshold. *Vision Res.* **39**, 2729–2737 (1999).

···

Monoclonal antibodies inhibit prion replication and delay the development of prion disease

Anthony R. White*, **Perry Enever***, **Mourad Tayebi***, **Rosey Mushens**†, **Jackie Linehan**‡, **Sebastian Brandner**‡, **David Anstee**†, **John Collinge***‡ & **Simon Hawke***

* CNS Infection and Immunity Group, Department of Neurogenetics, Division of Neurosciences and Psychological Medicine, Faculty of Medicine, Imperial College, Norfolk Place, London W2 1PG, UK
† IBGRL, National Blood Service, Bristol BS10 5ND, UK and ‡ MRC Prion Unit and Department of Neurodegenerative Disease, Institute of Neurology, University College London, Queen Square, London WC1N 3BG, UK

···

Prion diseases such as Creutzfeldt–Jakob disease (CJD) are fatal, neuro-degenerative disorders with no known therapy. A proportion of the UK population has been exposed to a bovine spongiform encephalopathy-like prion strain[1–3] and are at risk of developing variant CJD[4]. A hallmark of prion disease is the transformation of normal cellular prion protein (PrP^C) into an infectious disease-associated isoform[5], PrP^{Sc}. Recent *in vitro* studies indicate that anti-PrP monoclonal antibodies with little or no affinity for PrP^{Sc} can prevent the incorporation of PrP^C into propagating prions[6,7]. We therefore investigated in a murine scrapie model whether anti-PrP monoclonal antibodies show similar inhibitory effects on prion replication *in vivo*. We found that peripheral PrP^{Sc} levels and prion infectivity were markedly reduced, even when the antibodies were first administered at the point of near maximal accumulation of PrP^{Sc} in the spleen. Furthermore, animals in which the treatment was continued remained healthy for over 300 days after equivalent untreated animals had succumbed to the disease. These findings indicate that immunotherapeutic strategies for human prion diseases are worth pursuing.

Recombinant human PrP$^{91–231}$ folded into either α- or β-conformations[8,9] was used to produce monoclonal antibodies in mice lacking PrP (*Prnp$^{0/0}$*)[10] that are intolerant to PrP^C. ICSM 35, an immunoglobulin-γ2b (IgG2b) monoclonal antibody raised against β-PrP, with high affinity for both murine PrP^c and PrP^{Sc} (Fig. 1a; A. Khalili-Shirazi, S.H. and J.C., unpublished data), recognizes a region between amino acid residues 91 and 110 (ref. 11). ICSM 18 (isotype IgG1), raised against α-PrP, recognizes residues 146–159 of murine PrP and has a lower affinity for PrP^{Sc} (Fig. 1a). FVB/N mice were challenged intraperitoneally (i.p.) with Rocky Mountain Laboratory (RML) scrapie brain homogenate derived from terminally scrapie-sick mice and treated with ICSM 35, ICSM 18 or isotype control antibodies BRIC 126 (IgG2b) and BRIC 222 (IgG1) by twice weekly i.p. injection (2 mg per injection) from 7 or 30 days post inoculation (p.i.). Enzyme-linked immunosorbent assay (ELISA) analysis after 30 days of antibody treatment revealed no

significant differences between ICSM 35 or ICSM 18 antibody levels in the serum (Supplementary Information). Western blots of proteinase K-treated, phosphotungstic-acid-precipitated PrP^{Sc} from spleens of mice at 60 days p.i. revealed that treatment from 7 days p.i. with ICSM 35 or ICSM 18, but not with BRIC antibodies,
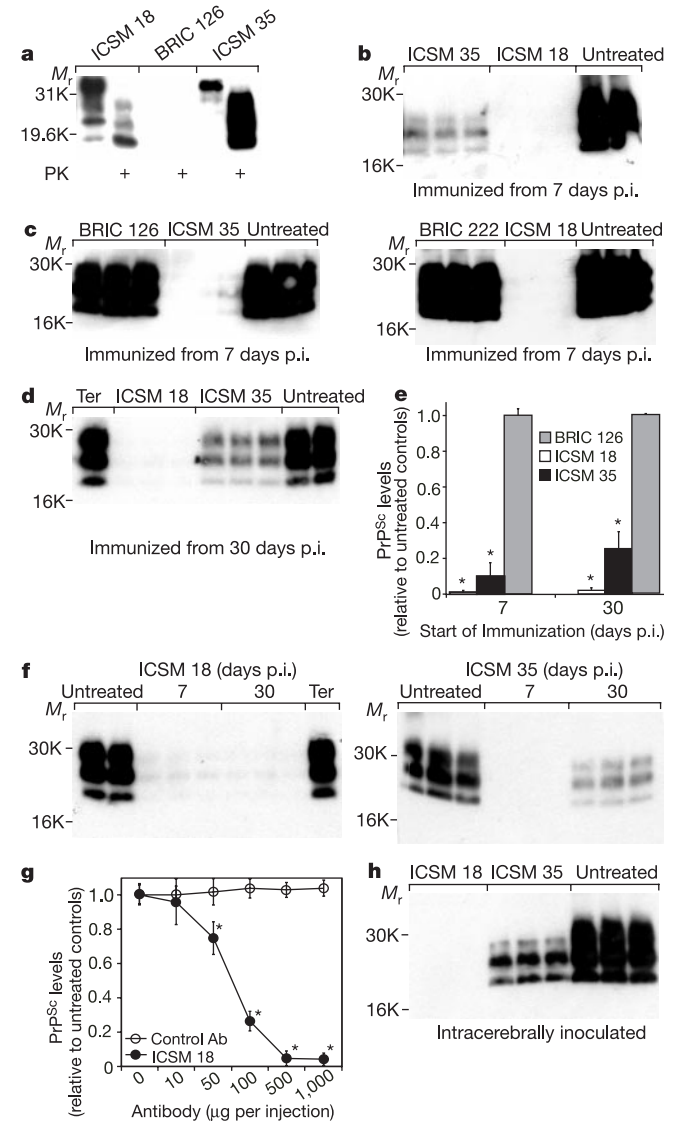

Figure 1 Anti-PrP antibodies inhibit splenic PrP^{Sc} protein levels. Western blots of proteinase K-digested, phosphotungstic-acid-precipitated PrP^{Sc} from spleens of mice 60 days p.i. with RML scrapie. Mice were inoculated i.p. except in **h**. Each lane contains PrP^{Sc} from an individual mouse. M_r, relative molecular mass; Ter, pooled splenic PrP^{Sc} from mice succumbing to terminal scrapie (195 ± 5 days p.i.). **a**, Immunoprecipitation of PrP from scrapie-infected mouse brain using ICSM or BRIC antibodies. PK, proteinase K. **b**, ICSM 18 and ICSM 35 induced substantial reductions in splenic PrP^{Sc} levels when treatment began from 7 days p.i., but this reduction was not seen in **c**, the BRIC-control-treated mice. **d**, ICSM 18 and ICSM 35 reduced splenic PrP^{Sc} when treatment began at 30 days p.i. **e**, Densitometry of PrP^{Sc} levels in the western blots. ICSM 18 induced greater reduction in PrP^{Sc} levels in spleens than ICSM 35, whereas BRIC 126 had no effect (asterisk, $P < 0.001$ compared with untreated spleens). **f**, ICSM 18 induced efficient clearance of PrP^{Sc} whether treatment began at 7 or 30 days p.i. ICSM 35 induced more efficient inhibition of PrP^{Sc} accumulation when treatment began at 7 days rather than 30 days p.i. **g**, ICSM 18 induced a dose-dependent reduction in PrP^{Sc} levels in spleens as determined by densitometry of western blots (asterisk, $P < 0.001$, ANOVA compared with control antibody (Ab) treatment). **h**, ICSM 18 and ICSM 35 inhibited splenic PrP^{Sc} accumulation in i.c. inoculated mice.